IEEE Open Journal of
Circuits and Systems

Received 25 June 2022; revised 15 September 2022; accepted 28 September 2022. Date of current version 24 November 2022.

Digital Object Identifier 10.1109/OJCAS.2022.3216928

A Nearly Interference-Free and Depth-Resolution-Configurable Time-of-Flight System Based on a Mega-Pixel Vertical Avalanche Photodiodes CMOS Image Sensor

SHOTA YAMADA (Member, IEEE), MOTONORI ISHII, SHIGETAKA KASUGA, MASATO TAKEMOTO, HIROMU KITAJIMA, TORU OKINO, YUSUKE SAKATA, MANABU USUDA, YUGO NOSE (Member, IEEE), HIROSHI KOSHIDA (Member, IEEE), MASAKI TAMARU, AKITO INOUE (Member, IEEE), YUKI SUGIURA, SHIGERU SAITO, TAIKI KUNIKYO, YUSUKE YUASA, KENTARO NAKANISHI, NAOKI TORAZAWA (Member, IEEE), TAKASHI SHIRONO, TATSUYA KABE, SHINZO KOYAMA, MITSUYOSHI MORI (Member, IEEE), YUTAKA HIROSE, MASAYUKI SAWADA, AKIHIRO ODAGAWA, AND TSUYOSHI TANAKA (Senior Member, IEEE)

Engineering Division, Panasonic Industry Company Ltd., Kadoma 5718506, Japan

This article was recommended by Associate Editor V. Chen.

CORRESPONDING AUTHOR: S. YAMADA (e-mail: yamada.shota@jp.panasonic.com)

ABSTRACT We present a long range (∼250 m) time-of flight (TOF) system with suppressed (nearly-free) mutual-interference. The system is based on a 1296 × 960 pixels vertical avalanche photodiodes (VAPD) CMOS image sensor (CIS). Real-time long-range 3D-imaging with 30 fps speed (450 fps for 2D imaging) is demonstrated. Designs and operation principles of the core circuits, i.e., a photon counting circuit and a global shutter driver, are fully described. The ranging method is based on a sub-range synthesis (SRS) where a range is set by the phase of exposure pulses with respect to that of the light source of the system. The depth resolution is configurable in that the minimum sub-range width limited by the light source pulse width of 10 ns or 1.5 m can be reduced to a 10 cm by introducing an indirect-TOF operation. Furthermore, by employing a random flight timing (RFT), mutual-interference in raw signal level is suppressed by 35 dB when 2 cameras are simultaneously operated. By simulation, the present system is estimated to be tolerant up to a case of 27 cameras operation.

INDEX TERMS Avalanche photodiode, vertical avalanche photodiode, time-of-flight, CMOS image sensor, photon counting, ranging, interference.

I. INTRODUCTION

Long range time-of-flight (TOF) sensors are highly expected for various applications such as automotive, surveillance and space systems [1], [2], [3], [4]. In these systems, a spatial (2D) resolution of 10 cm at 250 m, a depth (3D) resolution of about <10 cm in near range and a real time (30 fps or faster) imaging capabilities are fundamental requirements [2]. Also, the system performances should be guaranteed under severe environmental conditions such as at high/low temperatures and high background (sunlight ∼100 klux) conditions [5], [6]. In addition, another fundamental issue of mutual-interference between different systems operated in parallel should be resolved [1], [7]. Along these lines, single photon avalanche diodes (SPAD) CMOS image sensors (CIS) capable of single photon detection have been developed extensively in recent years [8], [9], [10]. Following the first Mega-pixel SPAD-CIS demonstration [11], a real-time 250 m ranging system utilizing "sub-range (SR)" synthesis approach based on a Mega-pixel vertical avalanche photodiode (VAPD) CIS realizing a 10 cm depth resolution in a near range (< 7 m) by direct- and indirect-mixed mode TOF has been reported [12]. As for sunlight tolerant systems, under a 117 klux sunlight condition, a stacked SPAD-CIS capable of ranging 200 m and 150 m for objects with reflectivity of 90 % and 10 %, respectively [13]. A similar performance of over 200 m ranging capability under a 70 klux sunlight environment has been reported by using an SiPM array integrated with hybrid analog-to-digital and time-to-digital converters [5]. As for the mutual-interference issue, by pulse position modulation (PPM), a DTOF system targeted for 28 dB suppressed interference has been proposed [1]. Together with PPM, by employing a double-pulse detection method, a DTOF system with suppressed mutual-interference has been reported [7]. Furthermore, by delaying the emission pulse, an ITOF system capable of suppressing interference is reported [14]. However, the issue is in general considered to remain because the maximum number of systems simultaneously operable under practical environmental conditions has not been clarified.

In this paper, firstly, we present the design and the performance verification of the 6 µm size and 1296 × 960 pixels VAPD-CIS including a photon counting pixel circuit and a global shutter driver. Secondly, we present a direct-indirect mixed mode TOF operation. The indirect mode is realized by phase-sensitive differentiation (PSD) on photon counts of two neighboring sub-ranges. This operation principle is essentially the same as that of conventional indirect-TOF CISs where phase difference between charge packets is obtained from different timings [15], [16]. Ranging capability up to 250 m with a lateral resolution of 10 cm and with a 10 cm depth resolution (7.4 cm precision and 1.4 cm accuracy) for near range is demonstrated. Thirdly, we describe a newly developed random flight timing (RFT) method suppressing mutual-interference as much as 35 dB. By experiments, simultaneous DTOF operation of 6 cameras with nearly-free mutual-interference is demonstrated under a room light condition. By simulation, we investigate the maximum simultaneously operable camera number. Under a condition of a 0.1 % rejection level, 27 cameras are found to be simultaneously operable.

II. DESIGN OF VAPD-CIS

A. ARCHITECTURE OF THE VAPD-CIS

In Fig. 1, architecture of the developed VAPD-CIS is schematically drawn. The pixel array consists of 1296 × 960 avalanche photodiodes operated with the Geiger-mode. Vertical circuits provide global exposure and reset pulses synchronous to the light source with a 100 kHz frequency through global shutter drivers (GSD) controlled by a global clock (GCK) from a phase-locked-loop (PLL) circuit. Readout circuits consists of the column amplifiers (COLAMP), correlated-double-sampling (CDS) and single-slope analog-to-digital converters (SS-ADC) connected to the horizontal shift register (HSR). It is noted that the number of bits after digitization is extended to 7 from the necessary photon counts (5 bits). The purpose of this extension is for a possible future upgrade. Finally, the series data are output via LVDS format in parallel (8 channels). The digital transfer speed of LVDS channels is 800 Mbps. The total power consumption is 2.2 W.

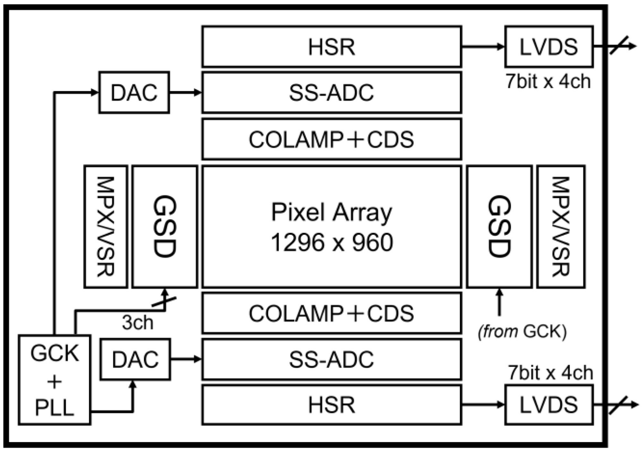

FIGURE 1. Architecture of VAPD-CIS.

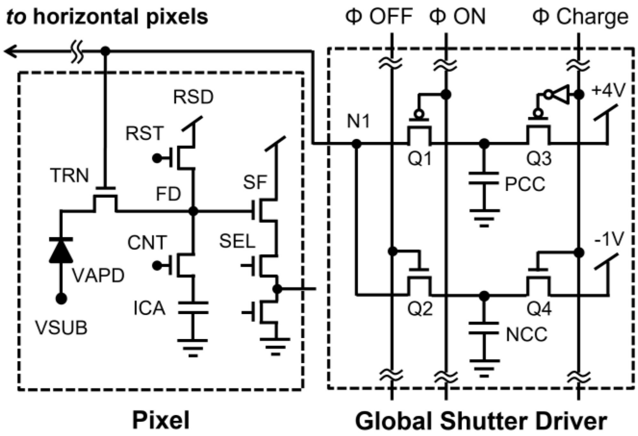

FIGURE 2. A schematic circuit diagram of one VAPD-CIS pixel and GSD. In each raw, two GSDs are arranged on both (left and right) sides of the VAPD pixel array.

B. PRECISION PHOTON COUNTING CIRCUITS

In Fig. 2, the pixel circuit diagram is illustrated. Each VAPD biased at −26.0 V (the excess voltage is 1.2 V) generates a Geiger-mode pulse on single photon absorption. The Geiger-mode pulse is self-quenched by charge storage on capacitors of VAPD itself and of stray components (capacitive quenching (CQ)) [17], [18], [19], [20], [21]. The stored charges after each single photon detection are used as a signal of one count of the photon. At a specified timing of each sub-range, generated charges of the Geiger-mode-pulse are transferred, by a transfer transistor (TRN), from a VAPD to the floating diffusion (FD) and then to the in-pixel charge accumulator ICA (a MIM capacitor) through the second transistor (CNT).

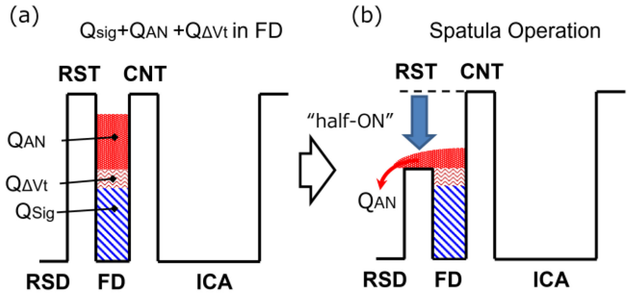

FIGURE 3. Potential diagrams of (a) before and (b) during charge packet spatula (CPS) operation. By subthreshold (denoted as "half-ON") biasing RST, the avalanche noise charge Q_{AN} are removed.

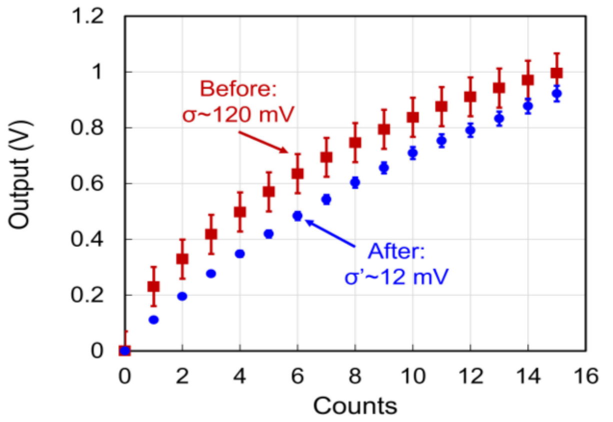

FIGURE 4. The output voltage of ICA as a function of counted number of pulses. Brown square dots with large error bars ($\sigma \sim 120$ mV) are obtained before a CPS operation. After a CPS operation, the blue circles with reduced error bars ($\sigma \sim 12$ mV) are obtained.

The accumulated charges suffer from two detrimental effects: (i) avalanche noise, Q_{AN}, and (ii) variation of the threshold voltage of each reset transistor (RST), $Q_{\Delta Vt}$, as shown in Fig. 3(a). In order to remove Q_{AN}, the reset transistor (RST) is operated in a sub-threshold regime (denoted as "half-on") skimming Q_{AN} as shown in Fig. 3(b). This operation mode is called charge packet spatula (CPS). As a result, the amount of charges is controlled to be identical in each pixel, typically, ∼2500 electrons. As shown in Fig. 4, with CPS, the variance is reduced to 12 mV from that without CPS, i.e., 120 mV. On the other hand, $Q_{\Delta Vt}$ is removed by a look-up table implemented in FPGA equalizing the scale of photon counts between the pixels, thus called photon counts equalizer (PCE). Histograms of a photon-count image before (dashed lines) and after (solid lines) PCE processing consisting of peaks due to 0 (dark count) to 15 photon counts are shown in Fig. 5. The improvement made by PCE is clear that the variance is reduced by more than a factor of 2. It is noted that significant improvement in the "0-count" peak after PCE operation is attributed to rejection of fixed pattern noise due other than to $Q_{\Delta Vt}$, additional function of PCE. It is noted that the capacitance value of ICA (15 fF) is critical. The dynamic range of ICA is 1.0 V. With this setting, the voltage amplitude of each photon count is much larger than that of kTC noises due to RST and CNT up to 15 counts. At room temperature, when the ICA capacitance is 15 fF, the kTC noise is about 2.0 mV, which is insignificant compared to the signal amplitude of 1 count, i.e., 22.5 mV $\sim$ 100 mV. Due to capacitive charge sharing effect, the voltage amplitude of the signal decrease. However, even in the worst case of the 15th photon count, the signal voltage amplitude is about 22.5 mV. On the other hand, the threshold voltage variation of RST in each cell is as large as 50 mV. Therefore, this is the major source of signal variation. Thus, since the RST-Tr threshold (Vt) variation contributes only to fixed pattern noise, this fixed pattern noise can be removed by holding it as a lookup table of PCE. It is noted that the effect of dark count ratio (DCR $\sim$ 100 cps at room temperature) is negligible for the above counting operation.

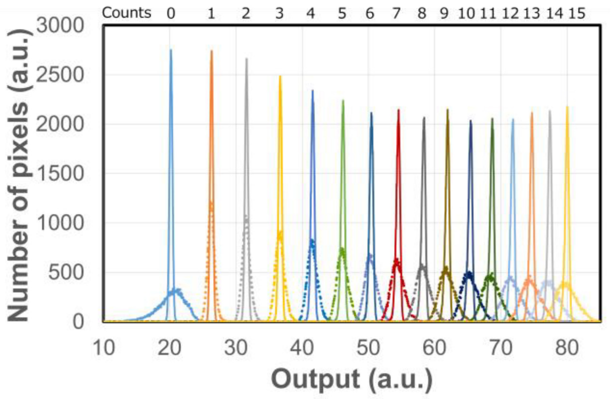

FIGURE 5. The photon-counting histograms before (dash line) and after (solid line) the photon counts equalizing (PCE) operation. The horizontal axis at the bottom is scaled with the output of VAPD-CIS. Corresponding photon counts are indicated at the top.

C. BIPOLAR-CAPACITANCE-PAIR (BCP)- BASED GLOBAL SHUTTER DRIVER (GSD)

For the direct-TOF operation, a global shutter as fast as 10 ns shutter-speed is required. If one followed a conventional shutter circuit design, one would need to drive 7.8 mm (= 6 μm × 1296 columns) long wires of 960 rows for transfer gates in all pixels in the short duration. This, in turn, requires a large power supply circuit and many high-power amplifiers. To avoid such high-power circuits, we developed a global shutter driver (GSD) driven by a bipolar-capacitor-pair (BCP). A circuit diagram of BCP-GSD is illustrated on the right side of Fig. 2. As illustrated in Fig. 1, BCP-GSDs are actually located on both sides of each raw. On both sides of each raw, the transfer gate line (TGL) of the raw is connected to a node, N1, switched either to a positively charged capacitor (PCC) or to a negatively charged capacitor (NCC). PCC and NCC are respectively, 8.2 pF and 8.1 pF. PCC is connected to N1 through a PMOS transistor (Q1) while NCC is through NMOS transistor (Q2). The gates of all Q1's are driven by ϕON signal generated by the global clock generator (GCK) simultaneously.

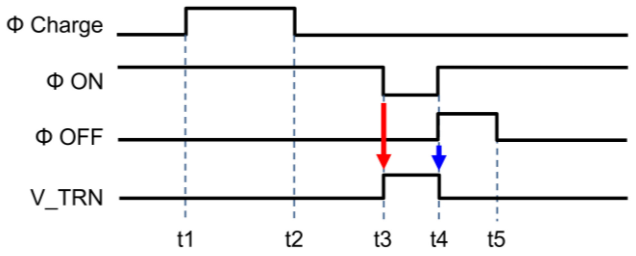

FIGURE 6. A schematic timing chart of BCP-GSD. ϕCharge, ϕON, and ϕOFF are supplied by the global clock generator (GCK) shown in Fig. 1. V_TRN is generated by trigger edges of positive (red arrow) and negative (blue arrow) chargings by PCC and NCC, respectively.

In the same manner, the gates of all Q2's are driven by ϕOFF signal also from GCK. PMOS transistor Q3 and NMOS transistor Q4 are connected to a positive (4V) power source and a negative (-1V) one to pre-charge, respectively, PCC and NCC. It is noted that all transistors on this diagram are made in a triple well structure to avoid the body-effect.

A schematic timing chart for this BCP-GSD is shown in Fig. 6. First, we assume that all the transfer gate lines are pre-charged to a ground level. Then, during a period of t1 to t2, PCC and NCC are pre-charged at 4V and -1V through Q3 and Q4, respectively, by a ϕCHARGE pulse. These values are higher than the nominal power supply voltage (3 V) and lower than the ground level (0 V), respectively, taking account of voltage drop due to the charge sharing effect between PCC/NCC and TGL. At the start of a global shutter operation, t3, the ϕON signal line is driven by a negative (from 3V-to-0V) pulse for a 10 ns through the PMOS transistor, Q1. By use of the PMOS turning-on operation, each transfer gate line is guaranteed to be charged to a full-turn-on voltage of the transfer transistors, TRN, within the CR-time constant of PCC/NCC and TGL, that is, 10 pF and 0.5 kΩ $\sim$5 ns. On the other hand, at the switching-off edge of Q1, t4, the ϕOFF signal line is turned on to discharge TGL by feeding the negative charges from NCC. In order to avoid a possible delay of turning-off operation of Q1's, the capacitance of NCC is set at slightly smaller (by 0.1 pF), than that of PCC. As a result, TGL's can be switched by a nominally 10 ns duration pulse, between t3 and t4 without using high power sources nor high power transistors. It is also noted that one does not have to wait until the complete settling time of the nominal 10 ns pulse. It is only necessary to turn on or off the transfer gate transistor. This means the transfer gate voltage has only to go across its threshold voltage, i.e., 0.5 V, resulting in an effective 10 ns "short-edge" shutter operation.

III. CONCEPTS OF THE SRS-TOF SYSTEM

A. SYSTEM ARCHITECTURE OF THE DEVELOPED TOF SYSTEM

A block diagram of the developed TOF system is illustrated in Fig. 7. Starting from the global clock (GCK), the random flight timing (RFT) is generated, and related control signals are supplied to VAPD-CIS, a photon light source, and to a post processor (FPGA). As described in Section II, the photon counts equalized by PCE are sent to the depth mapping engine and to the photon imaging engine generating 3D and 2D images, respectively, at the same time. Furthermore, the random flight timing (RFT) generator modulates the light emission and exposure timing randomly and reduces mutual-interference.

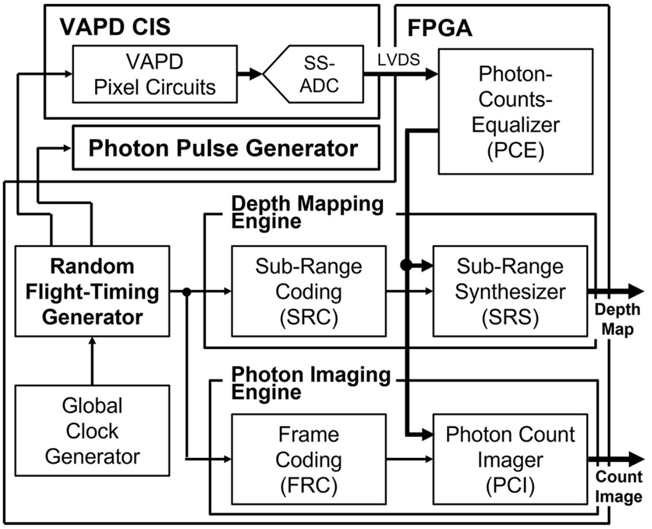

FIGURE 7. A block diagram of VAPD-TOF system consisting of main parts; VAPD-CIS, Photon Pulse Generator, and FPGA. Inside the main components, principal functional blocks are shown. Signal flows are indicated by bold arrows. Control signals are indicated by fine arrows.

B. CONCEPT OF SUB-RANGE-SYNTHESIS (SRS) METHOD

In Fig. 8, a concept of the present VAPD-TOF system is illustrated. Light pulses containing sufficient photons (about 18 µJ with wavelength of 940 nm) are repeatedly (100 kHz) emitted from a light source. Each pulse is reflected by an object located at a specific distance and detected by a TOF camera detector. The field of view (FoV) and the F number (F#) of the light source are, respectively, 30° × 10° and 1.0. The light source consists of a VCSEL array. The average energy/pulse is 18 uJ. The camera system is designed to be eye-safe satisfying the regulation, Class 1 of IEC 60825 [22]. Because the detector, a VAPD-CIS, is operated in a Geiger-mode [10], we classify the system as a direct-TOF system. However, determination of the distance or the range of an object is not based on a common time-to-digital converter (TDC) method but based on predetermined timing of a gated detection. A combination of gating timings divides a whole range into finite numbers of "sub-ranges" (Fig. 9(a)). In a conventional VAPD-TOF system [2], [21], the sub-ranges are measured sequentially by pairs of emission and detection pulses with fixed delay (T_d) for each sub-range (Fig. 9(b)). The minimum depth of the sub-range is determined by the width of the gating pulse, 10 ns (1.5 m). By synthesizing the sub-ranges images (sub-range synthesis:

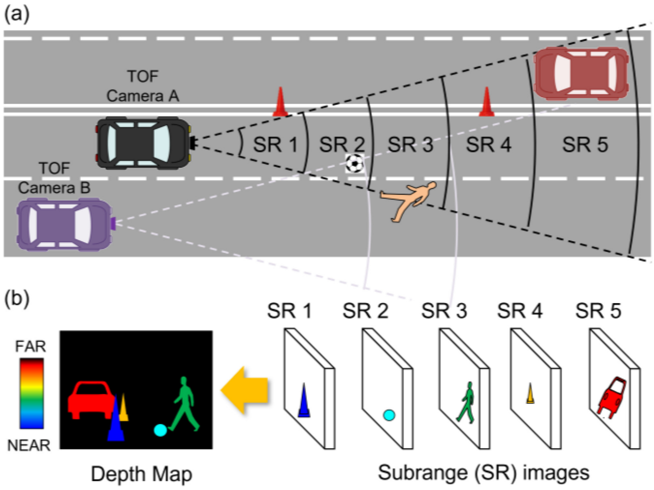

FIGURE 8. Concept of the direct-TOF sub-range-synthesis (SRS) method; (a) a schematic of an assumed usage scene on a road by two cars (TOF camera A and B). 5 sub-ranges each containing an object is shown. (b) a schematic of sub-range imaging and sub-range synthesis constructing a full range depth map.

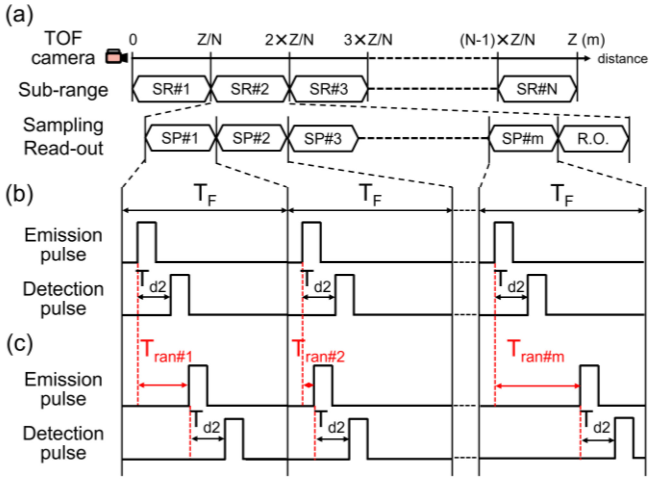

FIGURE 9. Timing charts of the SRS-TOF system; (a) A physical definition of a full range and its sub-ranges (top), a sequence of sub-range measurements (middle), and a sequence of flights (emission and detection pair) within a (2nd) sub-range (bottom). (b) A timing chart of repeated flights (emission and detection) with a fixed period in a sub-range. T_F represents the period of emission pulses (typically, 10μs corresponding to 100 kHz). (c) A timing chart with a random flight timing. The period of emission is modulated at each emission by a random amount.

SRS), a full range depth map is constructed as illustrated in Fig. 8 (b). It is noted that the distribution of the number of laser pulses is designed such that the maximum photon count number does not exceed 15 in each subrange. Therefore, a large number of laser pulses for a longer distance subrange is assigned than the one for a shorter distance subrange. Approximately, this number follows cubes of distance [21].

C. SUPPRESSION OF MUTUAL-INTERFERENCE BY RANDOM FLIGHT TIMING (RFT)

If two or more TOF cameras closely located each other are simultaneously operated (cameras A and B in Fig. 8 (a)), each camera would receive light pulses originally emitted from the other cameras as false signals. This is called mutual-interference (MI) effect. MI is a probabilistic event when detection pulses of different systems happened to overlap. In addition, in the conventional VAPD-TOF systems, the period of flight (pair of emission and detection) is identical to all the systems, the MI effect is enhanced due to the repeated detections.

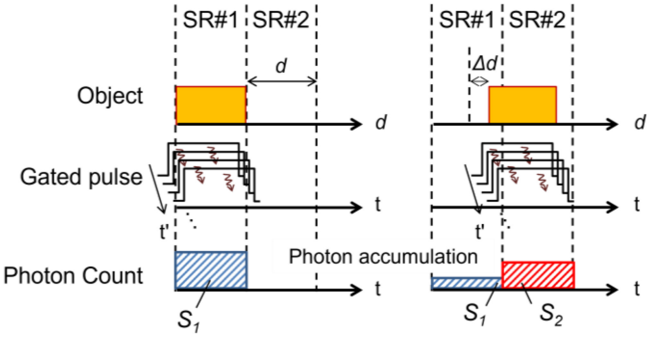

FIGURE 10. The schematic diagram of the phase differentiation in photon gating.

In order to avoid this repetition, we introduce two approaches. Firstly, following [1], the timing of flight (emission-detection pair) is randomly modulated within each sub-range measurement called random flight timing (RFT) (Fig. 9(c)). It is noted that effectiveness of this method is approximately proportional to the maximum number (m) of the randomly generated delay patterns. Approximately, m is described as

$$m \approx \frac{T_{ran}}{\Delta T_{del}} = \frac{\Delta\ B_{del}}{\Delta B_{ran}}, \tag{1}$$

where T_{ran} is the maximum delay duration and ΔT_{del} is the minimum possible delay period specified by the system clock. $1/T_{ran}$ and $1/\Delta T_{del}$ determine, respectively, effective bandwidths of the modulated flight timings (ΔB_{ran}) and of the randomly generated delay sequences ($\Delta\ B_{del}$). The third term is equivalent to the modulation index of the spread spectrum modulation and describes how the original interference signal is distributed to a wider bandwidth signal [1]. As explained in Section IV, typical value of m is 100 indicating suppression of mutual-interference by 40 dB

Secondly, by accumulating detection signals by repeated flights (typically 100 pulses) within each sub-range, and by thresholding the accumulated signal at a specified level, the confidence level of detection probability within each sub-range is enhanced. This is regarded as extension of the Prepost Histgramming of TDC method in [7].

D. PHASE DIFFERENTIATION IN PHOTON GATING

The depth resolution of the SRS-TOF system is ultimately determined by the width of the light source pulse. However, if one could obtain sufficient amount of pulse counts in each sub-range, it is possible to measure a displaced distance of an object from the center of the sub-range in a similar way as that of an indirect-TOF system (Fig. 10). Suppose an

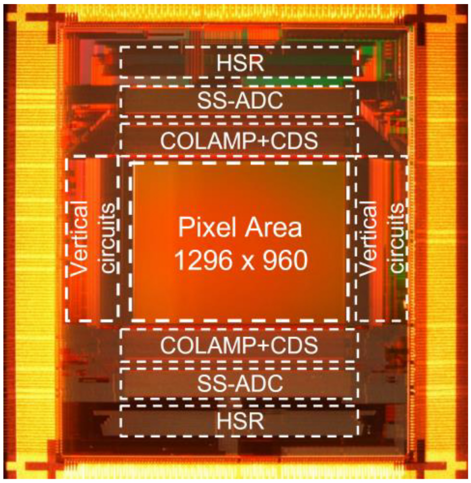

FIGURE 11. The chip photograph of the VAPD-CMOS image sensor.

object located near the boundary of a pair of two sub-ranges denoted as 1 and 2, the respective signals S_1 and S_2 from the object are detected in the two corresponding sub-range gating periods. The displacement of the object from the center of the assumed sub-range 1, Δd, can be obtained as

$$\Delta d = \frac{1}{2} \times d \times \frac{S_1 - S_2}{S_1 + S_2} \tag{2}$$

where d is the original sub-range depth, and S_1 and S_2 are photon counts obtained during gatings of sub-range 1 and 2, respectively. It is noted that S_1 and S_2 are numbers of photon counts in each sub-range. (The maximum value is 15 as shown in Fig. 4.) In order to enhance signal-to-noise ratio, when necessary, it is possible to increase these values by addition of sub-range frames after reconfiguration of pulse distribution within a full-range frame.

IV. EXPERIMENTAL RESULTS

A. CHIP PHOTOGRAPH

The designed VAPD-CIS is fabricated by a 65 nm 1P3M CMOS image sensor process customized with a MIM process for the in-pixel charge capacitor (ICA) explained in Section II-A. On-chip lenses are fabricated without visible-light color filters. In Fig. 11, a chip micrograph is shown. The die size is about 12.8 mm × 15.6 mm. The vertical circuit drivers including BCP-GSD described in Section II-C are located on both horizontal sides of the pixel area. The column circuits, column amplifiers, correlated double sampling (CDS) circuits, and SSADC's are located on both vertical sides of the pixel area. The digitized signals are transferred by horizontal shift register (HSR) circuit followed by 8 LVDS channels (not explicitly specified).

B. EVALUATION OF INDIRECT-TOF OPERATION

In Fig. 12, measurement results with the indirect-TOF mode described in Section III-D are shown. The measured range is from 5 m to 7 m. Displacements of 10 square wood bars with a 10 cm (horizontal) width were clearly measured. It is noted that these wood bars are located near the boundary of sub-range #4 (SR#4: hatched with blue) and sub-range #5 (SR#5: hatched with red). Precision and accuracy were, respectively, 7.4 cm and 1.4 cm. Considering the resolution of ADC, i.e., 7 bits, and the sub-range width of 1.5 m, this resolution is estimated to be about 1.2 cm. However, in this experiment, the resolution is limited by the total photon counts typically 15∼20 counts/sub-range conforming to the obtained resolution.

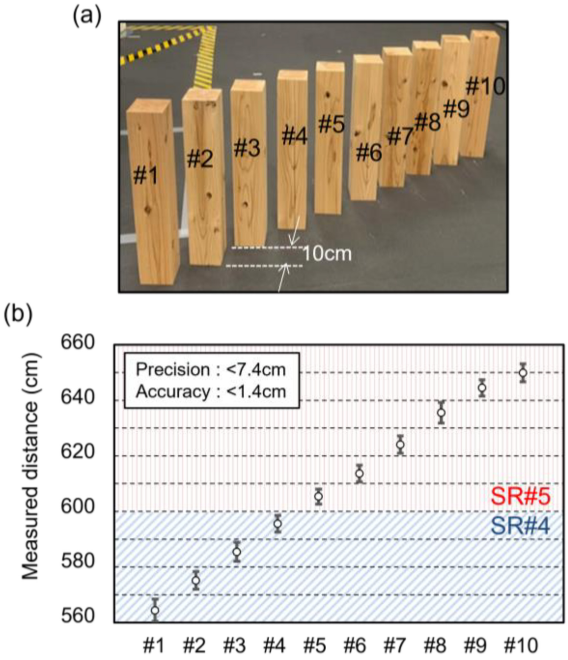

FIGURE 12. Demonstration of indirect-TOF operation by phase differentiating pulses from different subranges: (a) An intensity image captured by a common digital camera. The wood bars are 10 cm wide and located from 5.6 meter to 6.5 meter; (b) Measured distance of each wood bar as a function of location (numbers of bars). A 10cm depth resolution equivalent to the width of bar is resolved as indicated by the location of each measurement point separated by each 10 cm step ruler (dotted horizontal line). The vertical bar of each point is the precision (<7.4 cm).

C. DEMONSTRATION OF A LONG-RANGE DIRECT-INDIRECT-MIXED TOF OPERATION

Establishing the indirect mode TOF operation as described in the previous section, we performed a field test with the direct-indirect-mixed mode operation. The peak power of the light source is 1200 W. The full range is set from 30 m to 250 m. The background lighting condition is a nighttime with streetlights. A corresponding CIS image is shown in Fig. 13 (a). In Fig. 13 (b), a direct-TOF image is shown. The sub-range widths are set 3 m for a near range (< 48 m) and 22.5 m for a far range (> 48 m). Total number of the sub-ranges is 15. Each sub-range is clearly measured as expected. It is noted that in the third range set for 36 m to 39 m (specified by light blue color), apparently "one person" standing and spreading his or her both arms is observed near a solid block.

When the indirect-mode operation is set on, the depth resolution is improved as shown in Fig. 13 (c). The indirect-mode

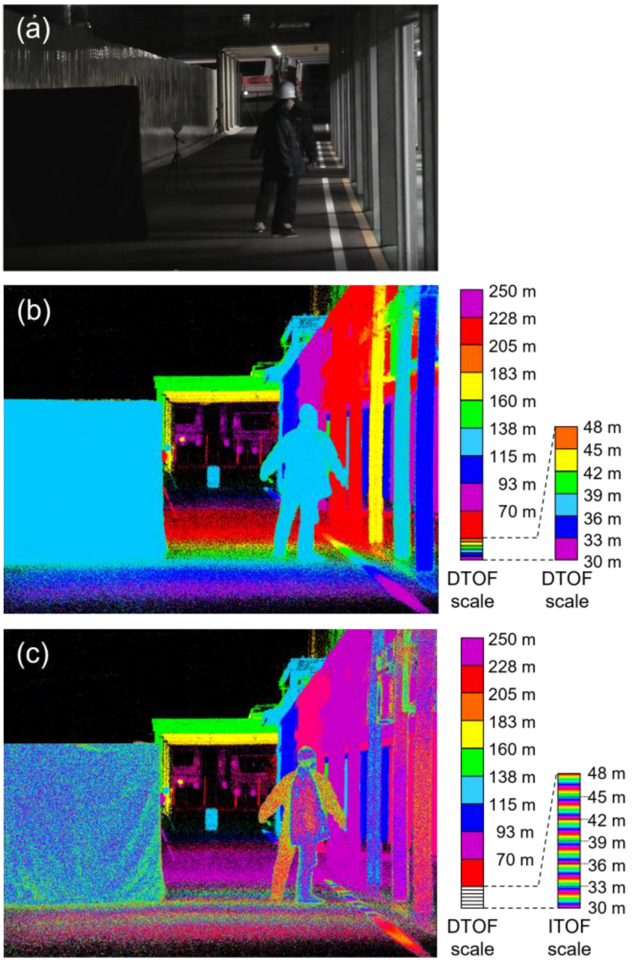

FIGURE 13. **A demonstration of a Geiger mode direct-indirect-TOF mixed image; (a) An intensity image captured by a common digital camera; (b) An ordinary Geiger mode direct-TOF image; (c) Geiger mode direct-indirect-mixed mode TOF image. The indirect-mode image in the near range (30 m-48 m) is generated by using lower 5 bits of an 8 bits color code resulting in a seeming 9 sub-ranges. The actual sub-range boundaries are indicated by the dotted lines on the right.**

operation is introduced only into the shorter range (< 48 m) without alternating the overall driving scheme explained in Fig. 9. In the experiment of Fig. 13(c), the exposure pulse width is 20 ns in the 3 m subrange of the six front ranges. As described in Section III-D, the indirect-mode improves the depth resolution within the 3 m sub-range by calculating Eq. (2) without changing the width of the emission and exposure pulses in the direct-mode. The difference is expressed by 15 counts of 300 cm, and the resolution is 20 cm (= 300/15). Corresponding to this 20 cm, one color is mapped. And 10 colors are used for each lap to express 200 cm. Therefore, the 18 m range from 30 m to 48 m is expressed by 9 laps (= 1800 cm/200 cm). By setting the indirect mode active, the apparent "one person" is clearly resolved into "two overlapped persons" facing two directions: one facing toward the camera and another facing to the right. Also, in the same sub-range, the solid wall was found to be covered by a wavy sheet. It should also be noted that both in Fig. 13 (b) and Fig. 13 (c), the long-range measurement performance is identical as indicated by the purple color image of the 250 m range.

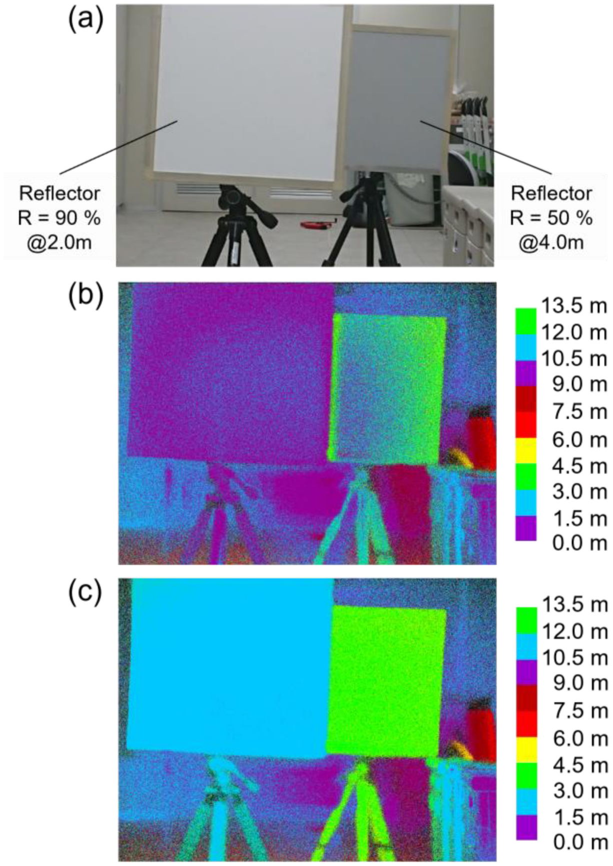

FIGURE 14. **A demonstration of mutual-interference free TOF mode image. Two cameras are operated simultaneously. The background light condition is 500 lux under a room light. (a) An intensity image captured by a digital camera; (b) Geiger mode direct-TOF image without RFT operation suffering from mutual-interference; (c) A normal Geiger mode direct-TOF image; with RFT operation showing nearly-free mutual-interference. All the TOF images are obtained by cutting the area of interest out of the full field of view (28°×21°) resulting in an apparent FoV of 20°×15°.**

Thus, a direct-indirect-mixed TOF sub-ranges synthesis all in one frame is realized.

D. DEMONSTRATION OF MUTUAL-INTERFERENCE FREE TOF OPERATION

For imaging suppressed mutual-interference, we set up two identical VAPD-TOF camera systems located side by side. The TOF-systems are operated in the direct-TOF mode. A scene with two reflectors with different reflectivity (90 % and 50 %) is prepared (Fig. 14 (a)). The background illumination condition is about 500 lux under a room light. The full range is from 0 m to 13.5 m with a constant depth resolution of 1.5 m set by the light source pulse of 10 ns.

In Fig. 14 (b), a full range depth map taken by one camera suffering interferences from another camera is shown. The reflector with a 50 % reflectivity located at 4.0 m exhibits color gradation (from light green (true sub-range) to light blue (false sub-range)). The reflector with a 90 % reflectivity also shows color variation from light blue (true

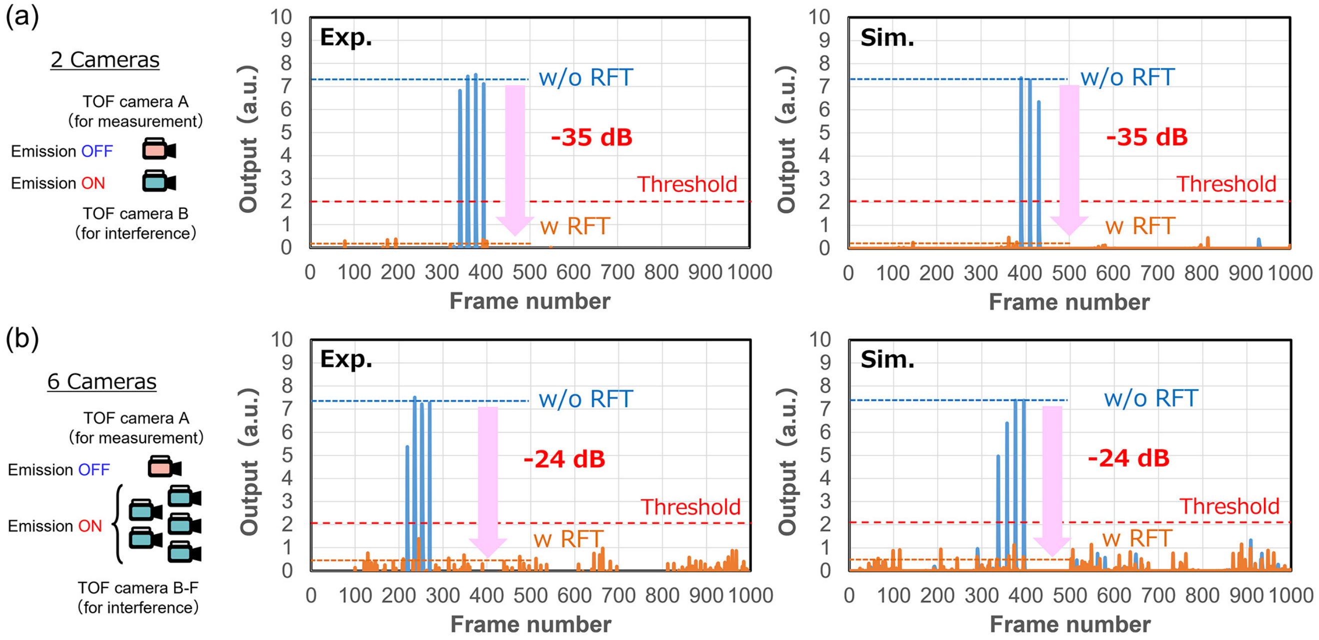

FIGURE 15. A demonstration of mutual-interference free TOF mode image; (a) Mutual-interference signals between 2 Giger mode direct-TOF cameras showing 35 dB reduction of MI by RFT operation by experiments (left) and by a simulation (right). (b) Mutual-interference signals between 6 Giger mode direct-TOF cameras showing 24 dB reduction of MI by RFT operation by experiments (left) and by a simulation (right).

sub-range) to purple (false sub-range). Considering the flatness of the reflectors' surfaces and the locations (centers of the sub-ranges), such color gradation should not be observed without interference. It is noted that such effect is probabilistic and obtained only occasionally.

With random flight timing (RFT) operation, depth images of reflectors are correctly obtained as light green for the reflector with 50 % reflectivity and as light blue for the reflector with 90 % reflectivity rejecting the interference (Fig. 14 (c)). It is emphasized that such correct image is obtained "constantly", indicating that the MI effect is nearly free due to "thresholding" operation during sub-range synthesis (SRS).

In order to confirm these points, and to analyze the maximum number of simultaneously operable systems, we analyzed the amount of interference signals corresponding to two and six simultaneous camera operations. In this experiment, the main camera (called camera A) is operated without emitting its own light pulses. Thus, camera A measures exclusively interference signals originated from other cameras. In Fig. 15, thus obtained interference signal levels are plotted as a function of time (frame number) for 2-cameras case (one interfering camera) (Fig. 15 (a)) and for 6-cameras case (5 interfering cameras) (Fig. 15 (b)). It is noted that 1000 frames out of much longer measurement frames are plotted. In each case, the physical experimental results are plotted on the left side and the simulation results are plotted on the right side. The simulation is implemented by emulating the actual RFT pulses and by evaluating the period of detection overlap between the master camera (camera A) and other interference sources. The reference levels corresponding to the signal due only to camera A itself are plotted as horizontal dotted blue lines in all graphs. With the conventional TOF scheme, i.e., without RFT, 3 ∼ 4 frames suffered from interference as high as the reference level plotted as solid blue peaks in both experiments. On activating the RFT operation, the effect of interference suppression is clearly obtained as the orange lines with low signal levels distributed in many frames. The effectiveness of reduction in the interference signal is estimated by calculating a reduction factor, i.e., decibel values of a ratio between the average output level without RFT (blue dotted line in the graphs) and the average output level with RFT (orange dotted line in the graphs). The reduction factor is obtained as 35 dB for the 2 cameras operation (Fig. 15 (a)), and 24 dB for the 6 cameras operation (Fig. 15 (b)). As clearly noticed from a comparison between the left- and right-side graphs, the experimental results quantitatively match with these simulation results. It is noted that, by sub-ranges synthesis (SRS), depth maps are created as binary images by thresholding the signal levels at the predetermined level (about 2 plotted as red horizontal lines in the graphs of Fig. 15). Thus, nearly free mutual-interference depth map images are obtained as demonstrated in Fig. 14 (c). It is also mentioned that the performance of RFT is not affected by the ambient light. This is because the background light only contributes as offsets of the photon counts in pixels uniformly.

Finally, using the same algorithm of the simulation, the effect of the present RFT method is investigated for cases of more (up to 30) cameras. In Fig. 16, the number of frames

TABLE 1. Chip and system performance summary and comparison with state-of-the-art APD-based and standard-PD CISs.

	This work	[13]	[11]	[1]	[18]	[23]	[24]
CMOS Technology	65 nm	90/40 nm	180 nm	45/65 nm	150 nm	65 nm	110 nm
Pixel Size	6 μm	10 μm	9.4 μm	19.8 μm	60 μm	7 μm	32 μm
2D Resolution	1296 x 960	189 x 600	1024 x 1000	256 x 256	64 x 64	640 x 480	64 x 64
Pixel Type	VAPD (=SPAD)	SPAD	SPAD	SPAD	SPAD	Standard-PD	APD
APD Mode	Geiger	Geiger	Geiger	Geiger	Geiger	N.A.	Linear
TOF type	Hybrid Direct and Indirect	Direct	Direct	Direct	Direct	Indirect	Indirect
Ranging Scheme	Direct: Photon Counting Indirect: Phase Difference	Time to Digital Converter	Photon Counting	Time to Digital Converter	Time to Digital Converter	4-tap phase sampling	APD-Gain Modulation
Maximum Range	250 m	300 m	1.6 m	150-430 m	367/5862 m	4 m	20 m
Accuracy	1.4 cm @6 m 1.5 m @250 m	< 15 cm	< 1cm	7-80 cm	1.5/35 m	N.A.	N.A.
Precision	7.4 cm @6 m	N.A.	< 7.8 mm	15-47 cm	20/50 cm	N.A.	2.1 cm
3D Frame Rate	30 fps	20 fps	N.A.	N.A.	7.68/7.16 fps	60 fps	96 fps
Suppression of interference	35 dB	N.A.	N.A.	28 dB	N.A.	N.A.	N.A.

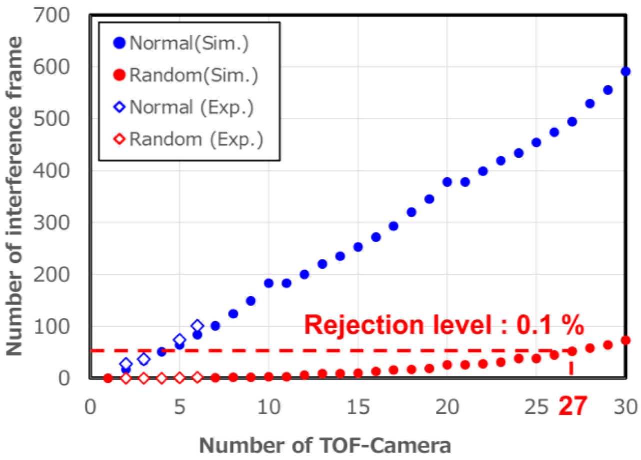

FIGURE 16. Number of interference frames a function of number of VAPD-TOF-cameras for without RFT (blue dots) and for with RFT (red dots). A rejection level of 0.1 % is plotted as a horizontal dotted line specifying the maximum number of simultaneously operable cameras.

obtained as "false" sub-ranges out of 50000 frames are plotted as a function of the number of simultaneously operated cameras. Blue dots are interference frames without RFT (w/o RFT), the red dots are interference frames obtained with the RFT method (w RFT). It is observed that, up to 15 cameras, the mutual-interference is almost negligible. If one set a rejection level of 0.1 % of false frame numbers, the present method is considered to be applicable to the case of simultaneous operation with 27 cameras as indicated in the graph.

V. CONCLUSION

We have presented a 1 Mega-pixel VAPD-CIS based TOF system with configurable depth resolution and with suppressed mutual-interference. Ranging method is determination of a sub-range in which an object is located. A full-depth map is constructed by sub-ranges synthesis (SRS). For long range (~250 m) measurement, a direct-TOF ranging mode is employed while for short range, indirect-TOF mode is realized by phase-sensitive-detection of photon count numbers between neighboring sub-ranges. With an ordinary direct-TOF mode, the depth resolution is set by the light source pulse, 1.5 m. With an indirect-TOF mode, a resolution down to 10 cm performing a 7.4 cm precision and a 1.4 cm accuracy is demonstrated in a near range (~6 m). In Table 1, the present VAPD-based TOF system is compared with state-of-the-art TOF systems. Two distinctive performances of the present system are: (1) a high lateral resolution due to a high pixel resolution; (2) a configurable depth resolution in "one frame" by mixed mode operation of direct-TOF and indirect-TOF. It should also be noted that the present system output 3D images in real time (30 fps) and 2D images with 450 fps.

Finally, a random flight timing (RFT) is introduced to suppress the mutual-interference. The effectiveness of the scheme is demonstrated by both experiments and simulations. Under moderate background lighting conditions

(500 lux), the method is found to be highly effective (raw signal suppression by 35 dB). By simulation, the method is estimated to be applicable to simultaneous operation of 27 cameras. The present system is considered to be suitable for various applications such as autonomous driving system, surveillance system of safety and security purposes.

REFERENCES

[1] A. R. Ximenes, P. Padmanabhan, M. J. Lee, Y. Yamashita, D. Yaung, and E. Charbon, "A 256 × 256 45/65 nm 3D-stacked SPAD-based direct TOF image sensor for LiDAR applications with optical polar modulation for up to 18.6 dB interference suppression," in *Proc. IEEE Int. Solid-State Circuits Conf. (ISSCC)*, San Francisco, CA, USA, 2018, pp. 96–98.

[2] S. Koyama et al., "A 220 m-range direct time-of-flight 688 × 384 CMOS image sensor with sub-photon signal extraction (SPSE) pixels using vertical avalanche photo-diodes and 6 kHz light pulse counters," in *Proc. IEEE Symp. VLSI Technol. Circuits*, Honolulu, HI, USA, Jun. 2018, pp. 71–72.

[3] M. E. Warren, "Automotive LIDAR technology," in *Proc. IEEE Symp. VLSI Technol. Circuits*, Kyoto, Japan, Jun. 2019, pp. C254–C255.

[4] E. Manuzzato, "A 64×64-pixel flash LiDAR SPAD imager with distributed pixel-to-pixel correlation for background rejection tunable automatic pixel sensitivity and first-last event detection strategies for space applications," in *Proc. IEEE Int. Solid-State Circuits Conf. (ISSCC)*, San Francisco, CA, USA, Feb. 2022, pp. 96–97.

[5] S. Kondo et al., "5.1 A 240 × 192 pixel 10fps 70klux 225m-range automotive LiDAR SoC Using a 40ch 0.0036 mm2 voltage/time dual-data-converter-based AFE," in *Proc. IEEE Int. Solid-State Circuits Conf. (ISSCC)*, San Francisco, CA, USA, Feb. 2020, pp. 94–95.

[6] S. Park, B. Kim, J. Cho, J. H. Chun, J. Choi, and S. J. Kim, "An 80×60 flash LiDAR sensor with in-pixel histogramming TDC based on quaternary search and time-gated Δ-intensity phase detection for 45m detectable range and background light cancellation," in *Proc. IEEE Int. Solid-State Circuits Conf. (ISSCC)*, San Francisco, CA, USA, Feb. 2022, pp. 98–99.

[7] H. Seo et al., "A CMOS LiDAR sensor with pre-post weighted-histogramming for sunlight immunity over 105 klx and SPAD-based infinite interference canceling," in *Proc. IEEE Symp. VLSI Technol. Circuits*, Kyoto, Japan, Jun. 2021. pp. 1–2.

[8] F. Villa et al., "CMOS imager with 1024 SPADs and TDCs for single-photon timing and 3-D time-of-flight," *IEEE J. Sel. Topics Quantum Electron.*, vol. 20, no. 6, pp. 364–373, Nov./Dec. 2014.

[9] N. A. W. Dutton et al., "11.5 A time correlated single photon counting sensor with 14 GS/s histogramming time to digital converter," in *Proc. IEEE Int. Solid-State Circuits Conf. (ISSCC)*, San Francisco, CA, USA, Feb. 2015, pp. 1–3.

[10] R. K. Henderson et al., "5.7 A 256 × 256 40nm/90nm CMOS 3D-stacked 120dB dynamic-range reconfigurable time-resolved SPAD imager," in *Proc. IEEE Int. Solid-State Circuits Conf. (ISSCC)*, San Francisco, CA, USA, Feb. 2019, pp. 106–108.

[11] K. Morimoto et al., "Megapixel time-gated SPAD image sensor for 2D and 3D imaging applications" *Optica*, vol. 7, no. 4, pp. 346–354, 2020.

[12] T. Okino et al., "5.2 A 1200×900 6μm 450fps geiger-mode vertical avalanche photodiodes CMOS image sensor for a 250m time-of-flight ranging system using direct-indirect-mixed frame synthesis with configurable-depth-resolution down to 10cm," in *Proc. IEEE Int. Solid-State Circuits Conf. (ISSCC)*, San Francisco, CA, USA, Feb. 2020, pp. 96–98.

[13] O. Kumagai et al., "7.3 A 189×600 back-illuminated stacked spad direct time-of-flight depth sensor for automotive LiDAR systems," in *Proc. IEEE Int. Solid-State Circuits Conf. (ISSCC)*, San Francisco, CA, USA, Feb.2021, pp. 110–111.

[14] K. Hatakeyama et al., "A hybrid indirect ToF image sensor for long-range 3D depth measurement under high ambient light conditions," in *Proc. IEEE Symp. VLSI Technol. Circuits*, Jun. 2022, pp. 46–47.

[15] S. Kawahito, I. A. Halin, T. Ushinaga, T. Sawada, M. Homma, and Y. Maeda, "A CMOS time-of-flight range image sensor with gates-on-field-oxide structure," *IEEE Sensor J*, vol. 7, no. 12, pp. 1578–1586, Dec. 2007.

[16] D. Kim et al. "5.4 A dynamic pseudo 4-Tap CMOS time-of-flight image sensor with motion artifact suppression and background light cancelling over 120 klux," in *Proc. IEEE Int. Solid-State Circuits Conf. (ISSCC)*, San Francisco, CA, USA, Feb. 2020, pp. 100–101.

[17] K. Zhao, S. You, J. Cheng, and Y. H. Lo, "Self-quenching and self-recovering InGaAs/InAlAs single photon avalanche detector," *Appl. Phys. Lett*. vol. 93, Jun. 2008, Art. no. 153504.

[18] M. Perenzoni, N. Massari, D. Perenzoni, L. Gasparini, and D. Stoppa, "A 160 × 120 pixel analog-counting single-photon imager with time-gating and self-referenced column-parallel A/D conversion for fluorescence lifetime imaging," *IEEE J. Solid-State Circuits*, vol. 51, no. 1, pp. 155–167, Jan. 2016.

[19] Y. Hirose et al., "A 400x400-pixel 6μm-pitch vertical avalanche photodiodes (VAPD) CMOS image sensor based on 150ps-fast capacitive re-laxation quenching (RQ) in geiger mode for synthesis of arbitrary gain images," in *Proc. IEEE Int. Solid-State Circuits Conf. (ISSCC)*, San Francisco, CA, USA, Feb. 2019, pp. 104–105.

[20] A. Inoue, T. Okino, S. Koyama, and Y. Hirose, "Modeling and analysis of capacitive relaxation quenching in a single photon avalanche diode (SPAD) applied to a CMOS image sensor," *Sensors*, vol. 20, no. 10, p. 3007, 2020.

[21] Y. Hirose et al., "A 250 m direct time-of-flight ranging system based on a synthesis of sub-ranging images and a vertical avalanche photo-diodes (VAPD) CMOS image sensor," *Sensors*, vol. 18, no. 11, p. 3642, 2018.

[22] *Safety of Laser Products—Part 1: Equipment Classification and Requirements*, IEC Standard 60825-1, 2014.

[23] M. Keel et al., "A 640 × 480 indirect time-of-flight CMOS image sensor with 4-tap 7μm global-shutter pixel and fixed-pattern phase noise self-compensation scheme," in *Proc. IEEE Symp. VLSI Technol. Circuits*, Kyoto, Japan, Jun. 2019, pp. 258–259.

[24] B. Park, I. Park, W. Choi, and Y. Chae, "A 64 × 64 APD-based ToF image sensor with background light suppression up to 200 klx using in-pixel auto-zeroing and chopping," in *Proc. IEEE Symp. VLSI Technol. Circuits*, Kyoto, Japan, Jun. 2019, pp. C256–C257.

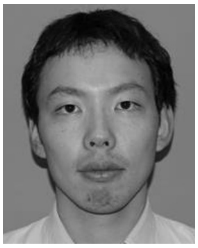

SHOTA YAMADA (Member, IEEE) received the B.Sc., M.Sc., and Ph.D. degrees in electronic engineering from Kyoto University, Japan, in 2008, 2010, and 2013, respectively. In 2013, he joined Panasonic Corporation. He has been engaged in development of CMOS image sensors and TOF camera-systems.

MOTONORI ISHII received the B.E. and M.E. degrees in electrical and electronic engineering, Kyoto University, Japan, in 1996 and 1998, respectively. He joined Panasonic Corporation and has been engaged in development of compound semiconductor devices, microwave devices, image sensors, and TOF sensing systems.

SHIGETAKA KASUGA joined Fujitsu Ltd., in 1988, where he was engaged in development of image sensors and memory devices. In 1997, he joined Matsushita Electric Industrial Company Ltd. (currently Panasonic Corporation), where he has been engaged in development of CCD camera modules and CMOS image sensors.

MASATO TAKEMOTO received the B.Sc. and M.Sc. degrees in information science and technology from the University of Tokyo, Japan, in 2002 and 2004, respectively. In 2004, he joined Semiconductor Company of Panasonic Corporation. He has been engaged in development of CMOS image sensors and camera-systems.

HIROMU KITAJIMA received the M.Sc. degree in engineering from the Nara Institute of Science and Technology, Japan, in 2020. In 2020, he joined Panasonic Corporation. He has been engaged in development of computer vision and robot learning.

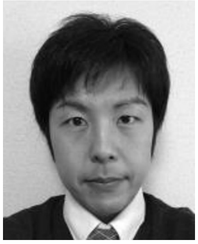

TORU OKINO received the B.S. degree in electrical/electronic and information engineering and the M.S. degree in quantum engineering from Nagoya University, Nagoya, Japan, in 2003 and 2005, respectively.

In 2005, he joined Matsushita Electric Industrial Company Ltd. (currently Panasonic), Osaka, and has been engaged in development of CMOS image sensors and imaging systems.

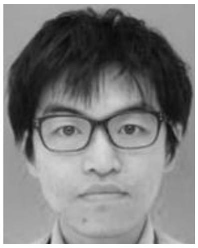

YUSUKE SAKATA received the B.Sc. and M.Sc. degrees in electronic engineering from Tokyo University, Japan, in 2007, and 2009, respectively. In 2009, he joined Panasonic Corporation and has been engaged in development of CMOS image sensors and TOF camera systems.

MANABU USUDA received the B.Sc., M.Sc., and Ph.D. degrees in physics from the Tokyo University of Science, Japan, in 1997, 1999, and 2002, respectively. From 2002 to 2004, he was a Postdoctoral Fellow with Synchrotron Radiation Research Center, Japan Atomic Energy Research Institute. In 2004, he joined Panasonic Corporation. He has been engaged in development of CIS devices and camera-systems.

YUGO NOSE (Member, IEEE) received the M.Sc. degree in electronic engineering from the Nara Institute of Science and Technology, Japan, in 2006. In 2006, he joined Panasonic Corporation and is currently engaged in development of CIS devices and camera-systems.

HIROSHI KOSHIDA (Member, IEEE) received the B.Sc. and M.Sc. degrees in electronic engineering from Kobe University, Japan, in 1994 and 1996, respectively. In 1996, he joined Matsushita Electric Industrial Company Ltd. (Panasonic Corporation) and is currently engaged in development of CIS and camera-systems.

MASAKI TAMARU received the B.Sc. degree in electronic engineering, in 1997. In 1997, he joined Matsushita Electric Industrial Company Ltd. (Panasonic Corporation) and is currently engaged in development of sensing systems.

AKITO INOUE (Member, IEEE) received the B.Sc. and M.Sc. degrees in applied physics from the University of Tokyo, Japan, in 2012 and 2014, respectively. In 2015, he joined Panasonic Corporation and is currently engaged in development of CIS devices and camera-systems.

YUKI SUGIURA received the B.E. and M.E. degrees from the Faculty of Science and Engineering, Waseda University, Japan, in 2007 and 2009, respectively. From 2009 to 2017, he developed semiconductor device and process technology with Toshiba Corporation. In 2017, he joined Panasonic Corporation and is currently engaged in development of CIS and Tactile sensors.

SHIGERU SAITOU received the B.Sc. and M.Sc. degrees in electronic engineering from Tohoku University, Japan, in 2004 and 2006, respectively. In 2006, he joined Panasonic Corporation, where he has been engaged in development of CIS devices, camera-systems, and image processing algorithms.

TAIKI KUNIKYO received the B.Sc. and M.Sc. degrees in engineering from Chiba University, Japan, in 2015 and 2017, respectively. In 2017, he joined Panasonic Corporation and has been engaged in development of CIS devices and camera systems.

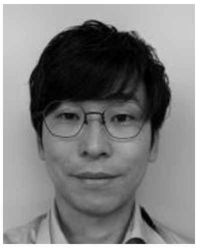

YUSUKE YUASA received the B.Sc. and M.Sc. degrees in engineering from the University of Tsukuba, Japan, in 2017 and 2019, respectively. In 2019, he joined Panasonic Corporation. He has been engaged in development of camera-systems and algorithms for artificial vision systems.

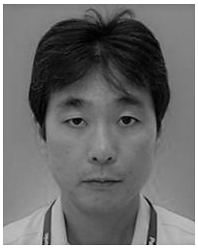

KENTARO NAKANISHI received the B.Sc. and M.Sc. degrees in electronic engineering from Osaka University, Japan, in 1993 and 1995, respectively. In 1995, he joined Panasonic Corporation and has been engaged in development of CIS devices, TOF systems, and MEMS devices.

NAOKI TORAZAWA (Member, IEEE) received the B.Sc., M.Sc., and Ph.D. degrees in material engineering from Nagoya University, Japan, in 2000, 2002, and 2017, respectively. In 2002, he joined Semiconductor Company of Panasonic Corporation. He has been engaged in development of CMOS devices, including CIS and photonic devices and systems.

TAKASHI SHIRONO received the B.Sc. and M.Sc. degrees in system engineering from Wakayama University, Japan, in 2002 and 2004, respectively. From 2005 to 2008, he was engaged in development of optical disc with Hitachi Maxell Corporation. In 2008, he joined Toshiba Corporation, where he was engaged in development of CIS and flash memory. In 2018, he joined Panasonic Corporation, where he has been engaged in development of CIS and piezoelectric devices.

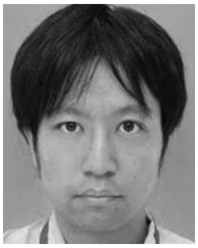

TATSUYA KABE received the B.Sc. and M.Sc. degrees in material engineering from Kyoto University, Japan, in 2004 and 2006, respectively. In 2006, he joined Panasonic Corporation and has been engaged in development of CMOS processes, 3-D integration, CIS, and photonic devices.

SHINZO KOYAMA received the B.Sc. and M.Sc. degrees in electronic engineering from Kyoto University in 2000 and 2002, and the Ph.D. degree in engineering from the Nara Institute of Science and Technology in 2017. In 2002, he joined Panasonic Corporation and has been engaged in development of CIS devices and camera systems.

MITSUYOSHI MORI (Member, IEEE) received the B.Sc., M.Sc., and Ph.D. degrees in electronic engineering from Osaka University, Osaka, Japan, in 1997 and 1999, respectively. In 1999, he joined Matsushita Electric Industrial Company Ltd., Osaka, Japan, and has been working on development of light-detecting devices and MEMS devices.

YUTAKA HIROSE received the M.E. degree from the University of Tokyo in 1987, and the Ph.D. degree from Princeton University in 1996. From 1987 to 1989, he was with NEC Laboratory working for optical disc systems. From 1996 to 2001, he was with Texas Instruments Japan and worked for DRAMs and CCDs. From 2001, he has been with Panasonic Corporation and engaged in GaN devices, THz devices, and CMOS imagers.

MASAYUKI SAWADA received the B.Sc. and M.Sc. degrees in electronic engineering from the Nagaoka University of Technology, Japan, in 1990 and 1992, respectively. In 2018, he joined Panasonic Corporation and is currently engaged in development of CIS and camera-systems.

AKIHIRO ODAGAWA received the B.Sc., M.Sc., and Ph.D. degrees in physics from Hiroshima University, Japan, in 1989, 1991, and 1999, respectively.

In 1991, he joined Panasonic Corporation and was engaged in oxide electronic material research like superconductor and magnetic material. From 1992 to 1995, he was a Researcher for superconducting devices with International Superconductivity Technology Center, Tokyo, Japan. From 2001 to 2003, he was a Senior Chief Researcher for ReRAM Memory Research with the National Institute of Advanced Industrial Science and Technology, Tsukuba, Japan. From 2011 to 2014, he was an On-Site Manager for Collaboration Research with Interuniversity Microelectronics Centre, Leuven, Belgium. Since 2015, he manages a research group working on development of image sensing systems.

TSUYOSHI TANAKA (Senior Member, IEEE) received the B.S. and M.S. degrees in applied physics and the Ph.D. degree in electrical engineering from Osaka University, Osaka, Japan, in 1983, 1985, and 2000, respectively. In 1985, he joined Matsushita Electric Industrial Company Ltd. (currently Panasonic Corporation), where he has been engaged in the research and development of GaAs high-speed/high-frequency devices, GaN high-frequency/terahertz/switching devices, semiconductor lasers, ReRAMs, TOF sensing systems and human sensing systems. He was awarded Okochi-Prize for the achievements on the world first industrialization of GaAs MMICs with on-chip BST (Barium Strontium Titanate) capacitors in 1995. He served as a Visiting Professor of Hokkaido University from 2006 to 2007. He is a Senior Member of Institute of Electronics, Information, and Communication Engineering of Japan.